***β*-MnO$_2$ nanostructures**, eventually decorated with Co_3O_4 or Fe_2O_3 nanoparticles, are grown by a plasma-assisted strategy on conductive glasses and porous Ni foams, and investigated as catalysts for the oxygen evolution reaction. The combined control over substrate properties and *β*-MnO_2 surface decoration yields outstanding functional performances, paving the way to real-world applications in sustainable energy conversion processes.

Keywords: MnO_2, Co_3O_4, Fe_2O_3, plasma-assisted fabrication, oxygen evolution reaction

Lorenzo Bigiani, Alberto Gasparotto, Chiara Maccato, Cinzia Sada, Johan Verbeeck, Teresa Andreu, Juan Ramón Morante, and Davide Barreca*

Dual improvement of *β*-MnO$_2$ oxygen evolution electrocatalysts *via* combined substrate control and surface engineering

ToC figure

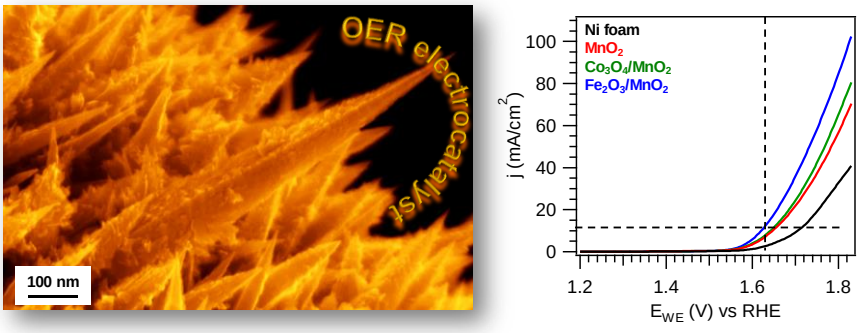

DOI: 10.1002/ ((please add manuscript number))
Article type: Full Paper

Dual improvement of β-MnO_2 oxygen evolution electrocatalysts *via* combined substrate control and surface engineering

Lorenzo Bigiani, Alberto Gasparotto, Chiara Maccato, Cinzia Sada, Johan Verbeeck, Teresa Andreu, Juan Ramón Morante, and Davide Barreca*

[*] Dr. L. Bigiani, Prof. A. Gasparotto, Prof. C. Maccato
Department of Chemical Sciences, Padova University and INSTM
35131 Padova, Italy
E-mail: alberto.gasparotto@unipd.it

Prof. C. Sada
Department of Physics and Astronomy, Padova University and INSTM
35131 Padova, Italy

Dr. T. Andreu, Prof. J. R. Morante
Catalonia Institute for Energy Research (IREC)
Sant Adrià de Besòs, 08930 Barcelona, Spain

Prof. J. Verbeeck
EMAT and NANOlab Center of Excellence, University of Antwerp, 2020 Antwerpen, Belgium

Dr. D. Barreca
CNR-ICMATE and INSTM, Department of Chemical Sciences, Padova University, 35131 Padova, Italy

Keywords: MnO_2, Co_3O_4, Fe_2O_3, plasma-assisted fabrication, oxygen evolution reaction

Abstract: The development of catalysts with high intrinsic activity towards the oxygen evolution reaction (OER) plays a critical role in sustainable energy conversion and storage. Herein, we report on the development of efficient (photo)electrocatalysts based on functionalized MnO_2 systems. Specifically, β-MnO_2 nanostructures grown by plasma enhanced-chemical vapor deposition on fluorine-doped tin oxide (FTO) or Ni foams were decorated with Co_3O_4 or Fe_2O_3 nanoparticles by radio frequency sputtering. Upon functionalization, FTO-supported materials yielded a performance increase with respect to bare MnO_2, with current densities at 1.65 V *vs.* the reversible hydrogen electrode (RHE) up to 3.0 and 3.5 mA/cm^2 in the dark and under simulated sunlight, respectively. On the other hand,

the use of highly porous and conductive Ni foam substrates enabled to maximize cooperative interfacial effects between catalyst components. The best performing Fe_2O_3/MnO_2 system provided a current density of 17.9 mA/cm^2 at 1.65 V *vs*. RHE, an overpotential as low as 390 mV, and a Tafel slope of 69 mV/decade under dark conditions, comparing favorably with IrO_2 and RuO_2 benchmarks. Overall, the control of β-MnO_2/substrate interactions and the simultaneous surface property engineering pave the way to an efficient energy generation from abundant natural resources.

1. Introduction

The ever increasing global energy demand and the dramatic environmental effects produced by the extensive use of fossil fuels have significantly promoted the interest in alternative technologies for sustainable energy production.[1-4] In this context, hydrogen (H_2) generation through electrochemical (EC) or photoelectrochemical (PEC) water splitting is considered a strategically promising option for the conversion of sunlight into a clean and carbon-neutral energy vector.[2,4-8] Actually, due to the sluggish kinetics and complex four-electron mechanism, the bottleneck limiting the overall process efficiency is the oxygen evolution reaction (OER), that requires the use of highly efficient and durable catalysts.[1,5-14] Up to date, the state-of-the-art systems are based on RuO_2 and IrO_2,[1,6-8,10,11,13,14] but their high cost and low natural abundance have stimulated the search for alternative eco-friendly, cheap and efficient (photo)electrocatalysts. In this scenario, manganese oxides (MnO_x) have emerged as appealing functional platforms for various processes and energy-related applications.[12,15-21] At variance with Ru and Ir oxides, MnO_x are naturally abundant, non-toxic and cheap materials[1,13,14,22] offering a large variety of crystal structures, that, combined with the rich redox and defect chemistry, yield a broad range of tunable chemico-physical properties.[2,5,8,23,24] Among manganese oxides, β-MnO_2 (*pyrolusite*) is the most thermodynamically stable MnO_2 polymorph, sharing with RuO_2 and IrO_2 the same rutile-type crystal structure.[6,11,25,26] *Pyrolusite* is an *n*-type semiconductor with a direct bandgap of ≈2.0 eV and favorable Vis-light absorption properties, along with strong adsorption and oxidation capabilities,[18,27,28] candidating it as an appealing OER (photo)electrocatalyst. Nevertheless, the more sluggish OER kinetics at the solid/liquid interface,[10,26] and lower electrical conductivity compared to RuO_2 or IrO_2,[6,22,25,26,29] render the optimization of the system properties an imperative task in view of practical utilizations.[1,2,9,14]

A promising strategy to overcome the first issue consists in MnO_2 surface decoration with highly dispersed nanoparticles (NPs) of suitable materials, that can improve charge separation

and transport, and beneficially influence the overall water oxidation efficiency.[22,30,31] So far, the functionalization of MnO_2 with metallic or oxide NPs has in fact enabled to achieve an enhanced electrocatalytic activity.[8,30-32] On the other hand, the problem of low conductivity can be mitigated by growing MnO_2 on porous and highly conductive scaffolds, enabling a more efficient catalyst-substrate contact and providing favorable pathways for mass/charge carrier diffusion.[5,13,33] Among the various options reported to date,[6,16] metallic nickel foams[13,33] positively combine a remarkable electrical conductivity with a high active area thanks to their continuous 3D porous network.[4,33]

In this study, the preparation of β-MnO_2-based OER electrocatalyst is performed for the first time by a two-step plasma processing route. Specifically, β-MnO_2 nanostructures are initially fabricated by plasma enhanced-chemical vapor deposition (PE-CVD) on both conventional fluorine-doped tin oxide (FTO)-coated glasses and porous Ni foams. The direct growth of the target material on these substrates yields a well-adherent deposit with an enhanced catalyst-support electrical contact, avoiding the inherent disadvantages of powder-processing techniques.[3,4,24,33,34] Subsequently, the obtained systems are decorated by radio frequency (RF)-sputtering with nanoparticles of Co_3O_4 or Fe_2O_3, chosen as prototypes of low-cost and active OER catalysts.[3,35-40] The infiltration power typical of the adopted plasma-assisted synthesis techniques[34,37,41-43] enables a very efficient dispersion of Co and Fe oxides into the pristine MnO_2 deposit, as well as an intimate contact between the nanocomposite constituents and the used substrates, critically affecting the resulting functional activity.[3,37,41-43]

The obtained systems were investigated as OER catalysts both in the dark and under simulated sunlight irradiation, devoting particular attention to the interplay between *pyrolusite* surface modification and catalytic activity as a function of the used substrate. The outcomes of this characterization highlighted outstanding (photo)electrochemical performances, whose occurrence and tailoring is rationalized in terms of cooperative electronic and chemical effects.

2. Results and Discussion

In the present study, MnO_2 nanostructures were initially grown by PE-CVD on FTO-coated glass substrates, widely used as standard supports for (photo)electrode materials,[17,27,44-46] and subsequently decorated with Co_3O_4 or Fe_2O_3 nanoparticles by means of RF-sputtering. The structure of bare and functionalized MnO_2-based samples was preliminarily investigated by X-ray diffraction (XRD, Figure 1a). The recorded patterns revealed the presence of peaks at $2\theta = 28.7°$ and 37.3°, attributable respectively to the (110) and (101) crystallographic planes of the β-MnO_2 polymorph.[19,47,48] No additional signals attributable to other manganese oxides could be observed, highlighting the formation of phase-pure systems. The broadness and weak intensity of β-MnO_2 diffraction peaks suggested the presence of small-sized crystallites with a highly defective structure, in line with previous literature reports on manganese oxide systems.[19,48,49] Concerning Co_3O_4/MnO_2 and Fe_2O_3/MnO_2 samples, the absence of XRD peaks originating from cobalt- or iron-containing phases could be attributed to the very low amount of the corresponding oxides, which were present as highly dispersed nanoparticles [37,50] (see below).

The occurrence of MnO_2 as the sole manganese-containing oxide was further confirmed by X-ray photoelectron spectroscopy (XPS), and, in particular, by the shape and position of Mn2p (Figure 1b) and Mn3s peaks (Figure S1a, Supporting Information), the latter being a fingerprint for the identification of the manganese oxidation state.[19,48,49] As far as the Co2p and Fe2p (Figures 1c-d) peaks are concerned, the position and separation of the two spin-orbit components supported the presence of Co_3O_4 and Fe_2O_3.[37,50]

Accordingly, the O1s peak (Figure S1b, Supporting Information) was characterized by a main contribution from lattice oxygen in MnO_2 and, eventually, Co_3O_4 or Fe_2O_3.[19,30,37,48,50] In addition, a second O1s component at higher BE values was attributed to the presence of surface hydroxyl groups chemisorbed on oxygen defects.[19,48,50,51] For composite systems, the higher concentration of the latter component suggested an increased amount of oxygen

defects with respect to bare MnO_2, that could beneficially affect catalytic performances (see below). For Co_3O_4/MnO_2 and Fe_2O_3/MnO_2 samples, calculation of the cobalt and iron surface molar fraction (see the Experimental section) yielded values of X_{Co} and X_{Fe} = 42% and 38%, respectively, indicating a comparable content of Co_3O_4 and Fe_2O_3 on the MnO_2 surface.

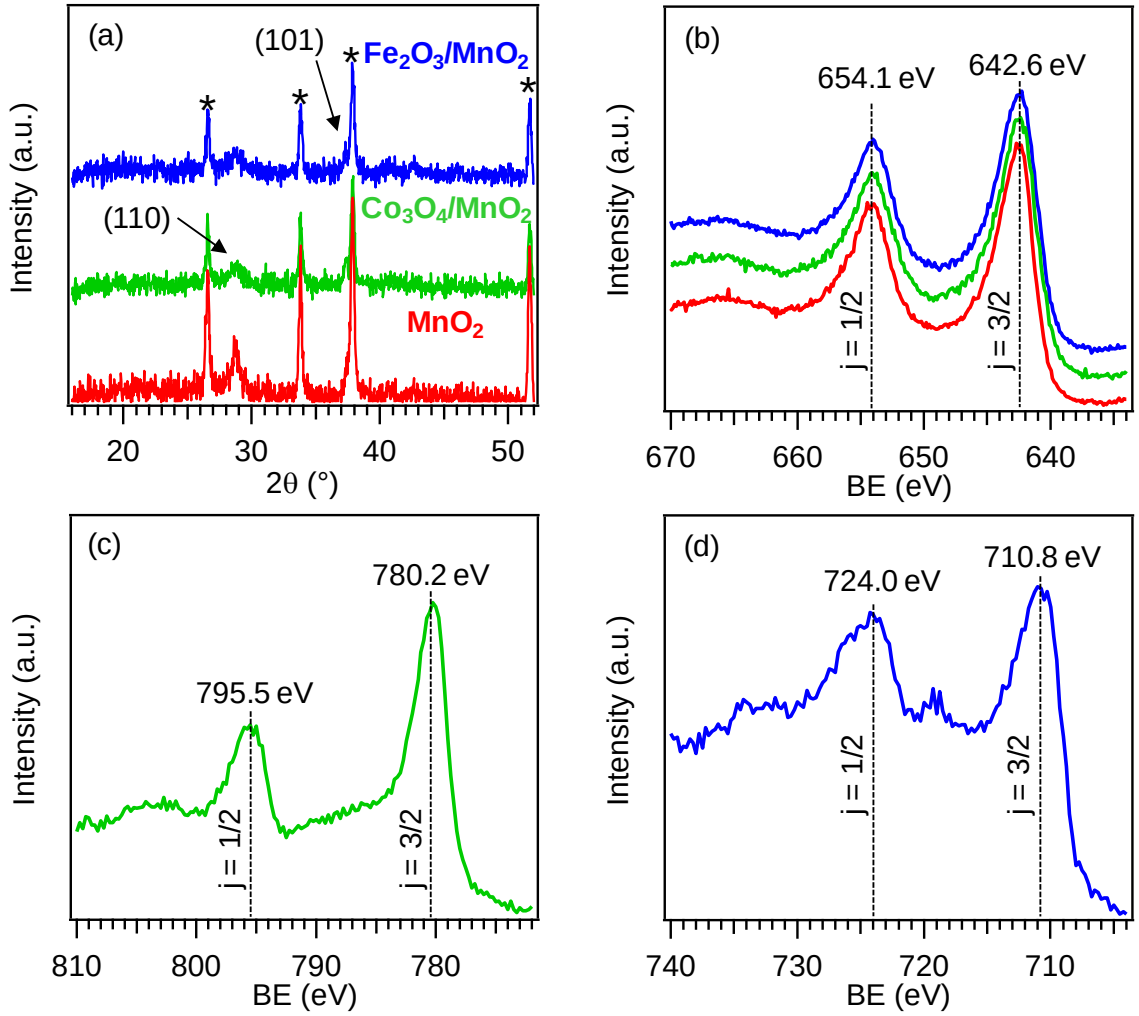

Figure 1. (a) XRD patterns for bare and functionalized MnO_2-based samples grown on FTO. Substrate reflections are marked by stars (*). XPS surface signals for Mn2p (b), Co2p (c) and Fe2p (d) regions. Color codes as in panel (a).

The in-depth composition of Co_3O_4/MnO_2 and Fe_2O_3/MnO_2 samples was investigated by secondary ion mass spectrometry (SIMS), devoting particular attention to the distribution of cobalt and iron oxides into MnO_2 (Figures 2a-b).

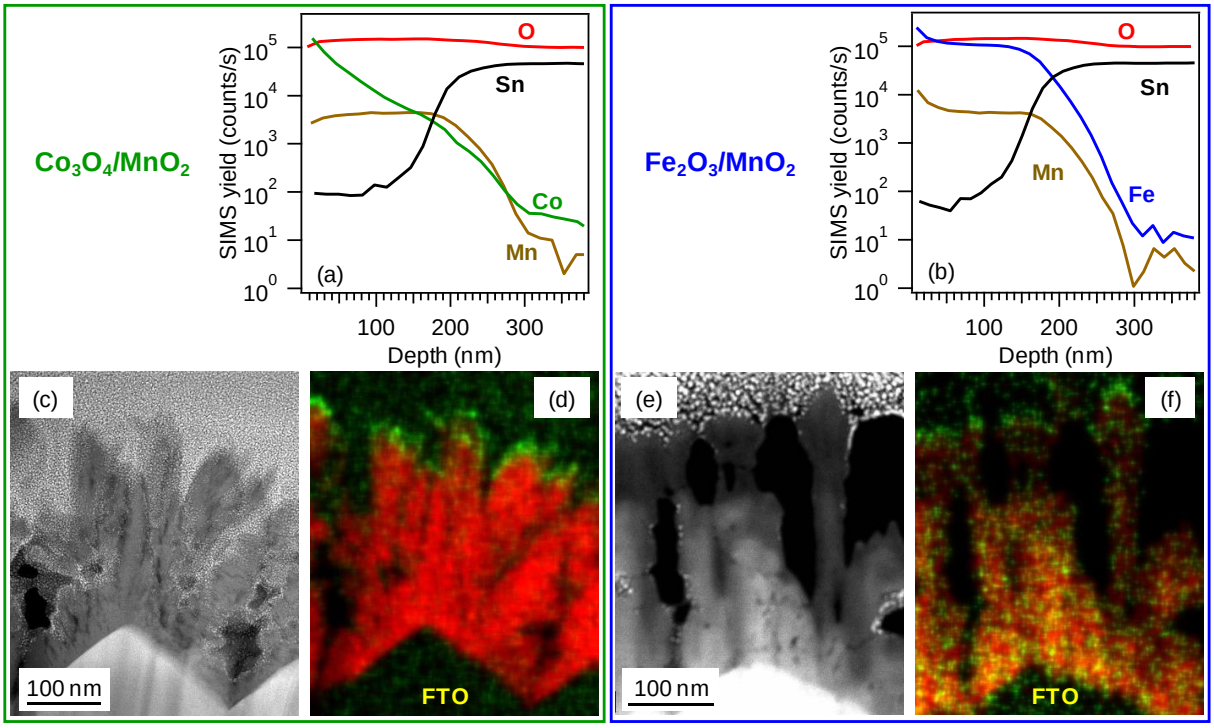

Figure 2. (a-b) SIMS depth profiles for Co_3O_4/MnO_2 and Fe_2O_3/MnO_2 samples supported on FTO. (c-d) Cross-sectional HAADF-STEM micrographs (left) and corresponding EDXS elemental maps (right) for the same specimen. Color codes: Mn = red; Co/Fe = green.

For both composite specimens, as well as bare MnO_2 (see also Figure S2, Supporting Information), manganese and oxygen ionic yields were nearly parallel from the surface up to deposit/substrate interface, suggesting a common chemical origin for such elements, in line with the presence of compositionally uniform MnO_2 deposits. Whereas for the Co_3O_4/MnO_2 sample the cobalt signal rapidly decreased as a function of depth, indicating that Co_3O_4 was mainly localized in the outermost deposit region, a more even distribution was revealed for the iron ionic yield in Fe_2O_3/MnO_2, pointing out to a high dispersion of iron oxide-containing species into MnO_2. In this regard, an additional important insight was gained by advanced TEM analysis. In particular, the combined cross-sectional analyses of functionalized samples by high angle annular dark field-scanning transmission electron microscopy (HAADF-STEM) and energy dispersive X-ray spectroscopy (EDXS, Figures 2c-f) revealed that the deposits (average thickness ≈ 250 nm) exhibited a porous morphology arising from the FTO substrate

coverage by elongated MnO_2 nanostructures with an irregular shape. In accordance with the previously discussed SIMS data, Co_3O_4 nanoparticles (typical particle size < 10 nm) appeared to be mostly concentrated in the outermost deposit region (green spots in Figure 2d), whereas Fe_2O_3 NPs (dimensions < 10 nm) were uniformly dispersed into MnO_2 (Figure 2f). These results indicate a different "wetting" behavior of MnO_2 by cobalt and iron oxides, in spite of the use of analogous sputtering conditions for manganese oxide decoration (see the Experimental section). The explanation for the different spatial distribution of Co_3O_4 and Fe_2O_3 nanoparticles into MnO_2 is not indeed a straightforward task, since it can be influenced by several concurring factors including the nature of species ejected from Fe and Co targets during the sputtering process and their interactions with the MnO_2 matrix, affecting, in turn, the subsequent nucleation events leading to the formation of cobalt and iron oxide NPs. Nonetheless, MnO_2 functionalization with Co_3O_4 or Fe_2O_3 did not alter the previous MnO_2 morphology, as revealed by plane-view and cross-sectional field emission-scanning electron microscopy (FE-SEM) images reported in Figure S3 in the Supporting Information. Overall, these results suggest the presence of a high density of Co_3O_4/MnO_2 and Fe_2O_3/MnO_2 heterojunctions, an important result to maximize beneficial cooperative effects among the system components in view of electrochemical applications.[3,37,41-43]

Since radiation harvesting by the target materials is of utmost importance for PEC applications, bare and functionalized MnO_2 samples were investigated by optical absorption spectroscopy (Figure 3). All specimens displayed similar spectra, indicating that the functionalization with Co_3O_4 or Fe_2O_3 did not induce any significant spectral modification, in line with the presence of MnO_2 as the main system component. All the spectra reported in Figure 3a are characterized by an appreciable radiation absorption throughout the Vis region, consistently with the almost black color of the present samples (see inset in Figure 3a) and by a progressive absorbance increase at lower wavelengths related to electronic interband transitions. Correspondingly, Tauc plot analysis yielded a band gap value E_G of ≈2.0 eV

(Figure 3b).[11,19]

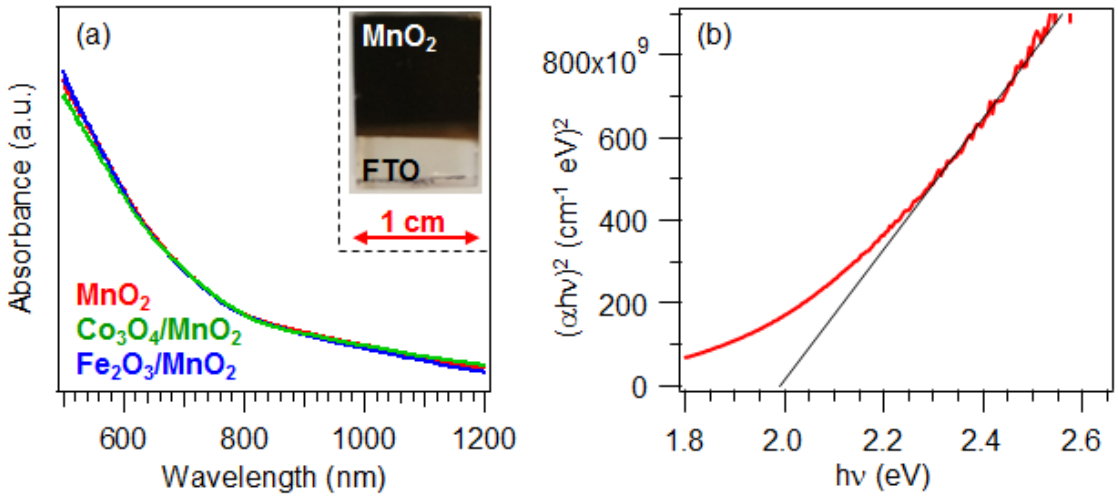

Figure 3. (a) Optical absorption spectra for MnO_2-based specimens on FTO substrates. The inset displays a digital photograph for a representative sample. (b) Tauc plot for bare MnO_2.

FTO-supported specimens were hence investigated as OER catalysts in (photo)electrochemical water splitting, collecting linear sweep voltammetry (LSV) curves both in the dark and under simulated solar irradiation (see the Experimental section). The anodic dark currents reported as dotted lines in Figure 4a clearly reveal that MnO_2 decoration by cobalt and iron oxide yielded improved electrochemical performances, with current densities increasing in the order MnO_2 < Co_3O_4/MnO_2 < Fe_2O_3/MnO_2. In particular, values of 1.6, 2.5, and 3.0 mA/cm^2, respectively, were obtained at 1.65 V *vs.* the reversible hydrogen electrode (RHE). Such results compare favorably with a large part of literature data on various manganese-based materials (films, powders and composites of different MnO_x polymorphs) and are among the highest ever reported for MnO_2-based systems (see Table S1), highlighting the potential of the proposed fabrication approach for the obtainment of highly efficient nanocomposite photoelectrodes.

The improved activity of functionalized samples can be traced back to the synergistic concurrence of different phenomena. In particular, the formation of heterojunctions at Co_3O_4/MnO_2 and Fe_2O_3/MnO_2 interfaces, as evidenced by the intimate contact between the

system constituents (see the above reported SIMS and TEM data), enable an improved separation of photogenerated charge carriers,[52] suppressing detrimental recombination phenomena and resulting in a higher photoactivity. Additional contributions arise from the intrinsic catalytic activity of cobalt and iron oxides toward OER,[38,39,53] further enhanced by the higher oxygen defect content on surface-decorated MnO_2-based systems (see the above XPS data).[17]

The process kinetics was investigated through the analysis of Tafel plots (Figure S4, Supporting Information), revealing that Tafel slope values in the dark decreased in the order: MnO_2 > Co_3O_4/MnO_2 > Fe_2O_3/MnO_2. Such a trend confirms the beneficial effect of MnO_2 functionalization, since lower slope values are related to a higher catalytic activity.[44]

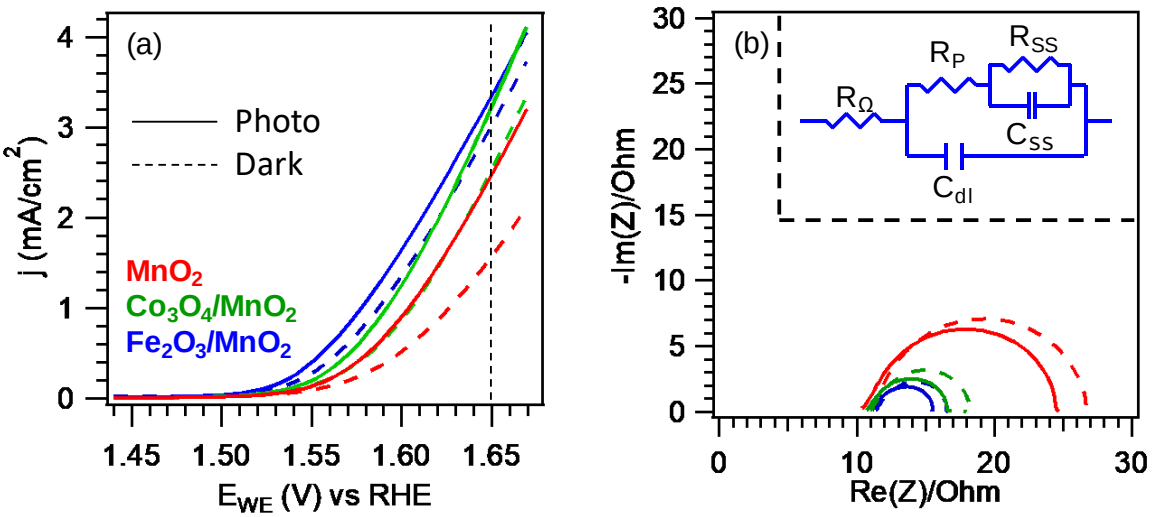

Figure 4. (a) LSV curves (under dark and irradiation) for bare and functionalized MnO_2-based samples supported on FTO. (b) Nyquist plots for the same specimens. The inset shows the equivalent circuit model used to fit the experimental data. The corresponding fitting parameters are reported in Figure S5 in the Supporting Information.

In order to attain a deeper insight into dark OER performances of the target systems, electrochemical impedance spectroscopy (EIS) measurements were carried out (dotted curves in Figure 4b), and the obtained experimental data were fitted assuming that charge transfer is mediated by surface states, according to a previously reported equivalent circuit model.[54-58]

(see inset to Figure 4b and Figure S5, Supporting Information). The resistance in the high frequency region, related to the series resistance (R_Ω), which includes electrolyte, electrodes and electric contacts, [54-58] was ≈11 Ω cm^2. In addition, for the three specimens, Nyquist plots yielded a similar trend for both polarization resistance R_P (the total charge transfer resistance associated to the multiple OER steps) and R_{SS} (related to the production rate of surface intermediates during OER).[59,60] In particular, the obtained R_P and R_{SS} values were lower for composite samples in comparison to bare MnO_2 (see table in Figure S5, Supporting Information). Charge transfer efficiency at the semiconductor electrolyte interface (SEI) through surface states can be estimated taking into account the charge transfer resistances, which were considered to be inversely proportional to the rate constants:[56-58]

$$Transfer\ efficiency(\%) = \frac{k_{SS}}{k_{SS}+k_P} \times 100 = \frac{R_P}{R_{SS}+R_P} \times 100 \quad (1)$$

where k_P and k_{SS} are the kinetic rates for charge transfer through the bulk of the semiconductor and the surface states, respectively. Decoration with Co_3O_4 or Fe_2O_3 results in a much higher transfer efficiency (31% and 38%, respectively) compared to pristine manganese dioxide nanostructures (18%). On the other hand, capacitance values both at the semiconductor (C_{dl}) and at the surface states (C_{SS}) increase in the order MnO_2 < Co_3O_4/MnO_2 < Fe_2O_3/MnO_2, which can be attributed to a higher carrier density.

Overall, results indicate that decoration of manganese dioxide nanostructures with Co_3O_4 or Fe_2O_3 yielded: i) a superior charge transfer rate, ascribed to a higher charge carriers density,[45] and an improved charge carriers separation[35] occurring upon heterojunction formation;[52,61] ii) an easier formation of active species boosting the overall OER efficiency, thanks to the higher concentration of oxygen defects and the intrinsic catalytic activity of Co_3O_4 and Fe_2O_3.[2,17,62,63]

Interestingly, upon irradiation with simulated solar light, the photocurrent density curves in Figure 4a revealed an increase according to the same order observed under dark conditions,

but yielding higher current densities of 2.4, 3.2, and 3.5 mA/cm^2 at 1.65 V *vs*. RHE for MnO_2, Co_3O_4/MnO_2, and Fe_2O_3/MnO_2, respectively (see also Figure S6, Supporting Information), and lower Tafel slope values (Figure S4, Supporting Information). In this regard, EIS data under irradiation (see Figure 4b and Figure S5, Supporting Information) showed a decrease of R_P and R_{SS} values with respect to the corresponding dark values. These results could be explained considering that electron/hole generation resulting from material illumination could improve charge transfer rate (higher $R_P/(R_{SS}+R_P)$ ratio of 19% for MnO_2, 34% for Co_3O_4/MnO_2, 42% for Fe_2O_3/MnO_2) thanks to a higher availability of electroactive species.[45] In addition, photogenerated electrons can induce a partial reduction of Mn(IV) to Mn(III) under illumination[51,64-68] which, in turn, can enhance OER kinetics thanks to the weakening of metal-oxo bonds (lower R_{SS}).[44,46] Overall, the present data reveal that the developed MnO_2-based materials can act as highly efficient platforms for eventual photoelectrochemical applications.

Based on the promising results obtained for FTO-supported specimens, the deposition of analogous MnO_2-based systems was subsequently carried out on Ni foams, with the aim of investigating if, and how, the unique characteristics of such substrates could beneficially affect the system electrochemical performances. In this regard, Figure 5a reports a FE-SEM micrograph of a bare MnO_2 system on Ni foam, whose morphology clearly differs from the corresponding samples on FTO (Figure S3, Supporting Information). In fact, highly porous arrays of quasi-1D MnO_2 nanothorns (length comprised in the range 200 nm - 2 μm) protruding from a relatively compact underlayer were observed in the present case. A similar sample morphology was observed also for Co_3O_4- and Fe_2O_3-decorated systems (Figure S7, Supporting Information). Such 1D nanostructures are of particular applicative interest since they offer a direct axial pathway for electron collection by the underlying substrate, along with short radial distances for hole transfer,[17,69] yielding thus improved charge transport properties.

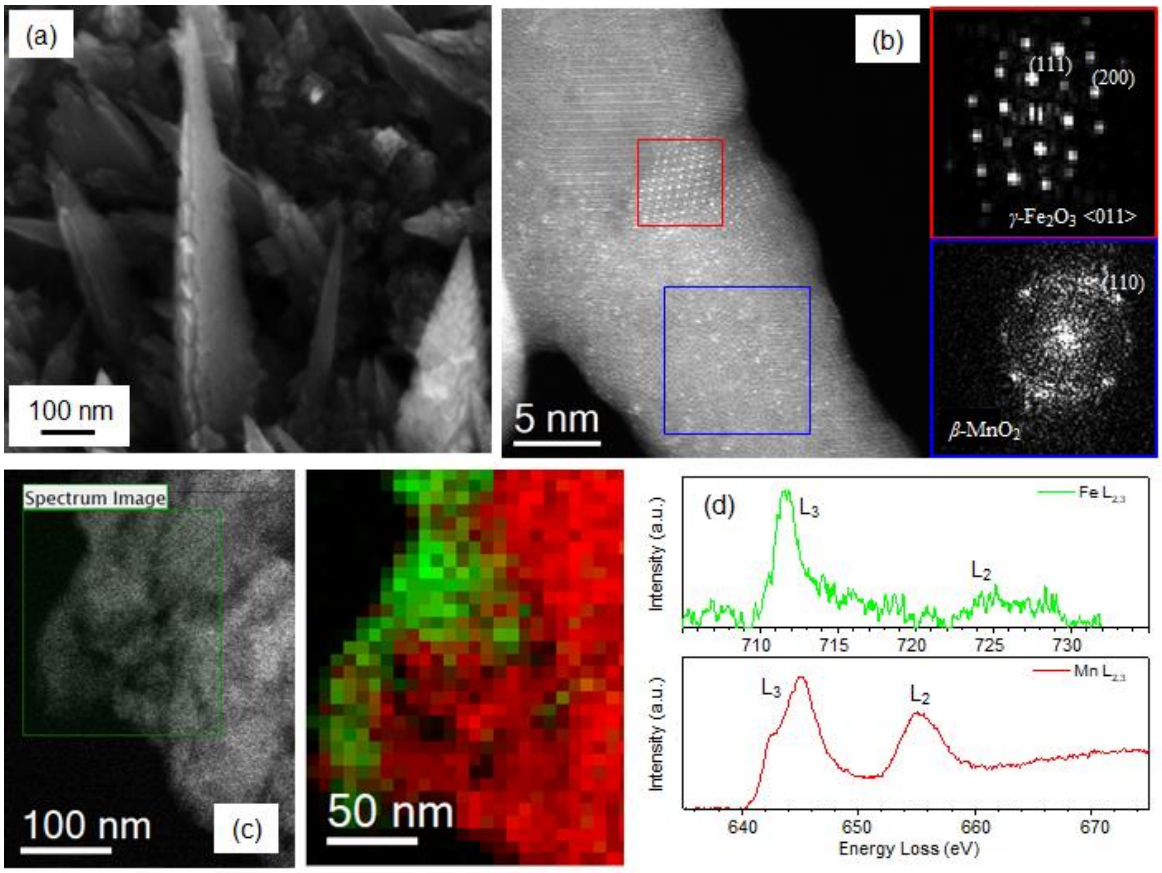

Figure 5. (a) Plane-view FE-SEM image of a bare MnO_2 sample grown on Ni foam. (b) HR-TEM micrograph of Fe_2O_3/MnO_2 on Ni foam and corresponding patterns obtained by the Fourier transforms of the regions highlighted by the red and blue boxes. (c) EELS analysis on the iron-rich region highlighted by the green box in the HAADF-STEM image (color codes: Mn = red; Fe = green) and (d) corresponding Fe $L_{2,3}$ and Mn $L_{2,3}$ edge EELS spectra.

Figure 5b reports a high resolution- (HR-) TEM image of the Fe_2O_3/MnO_2 sample on Ni foam along with selected area electron diffraction (SAED) patterns collected on the regions highlighted by red and blue boxes. Nanothorns were formed by the β-MnO_2 phase, consistently with the above XRD results on FTO-supported samples (see Figure 1a). From the high resolution HAADF image and average SAED diffraction patterns, we confirm the presence of β-MnO_2 phase[47] in polycrystalline form, with an approximate grain size of the order of 10 nm and no preferential average orientation. In addition, low-sized γ-Fe_2O_3[70] nanoparticles with an average diameter of ≈ 5 nm were also detected, despite other regions revealed the presence of larger Fe_2O_3 aggregates (see Figure 5c and Figure S8, Supporting

Information). The formation of the γ iron(III) oxide polymorph, instead of the most stable α one, was traced back to the non-equilibrium plasma conditions characterizing RF-sputtering.[71] Electron energy loss spectroscopy (EELS) analysis on the iron-rich regions (see Figure 5c) confirmed that manganese and iron formed physically distinct phases and were present as Mn(IV) and Fe(III) species, respectively (Figure 5d).[72]

The electrochemical performances of bare and functionalized MnO_2-based samples on Ni foam were finally tested in the OER process (Figure 6). As can be observed, all the materials yielded current densities in the dark higher than the homologous FTO-supported ones (compare Figures 6a and 4a). This improvement might be ascribed to the metallic conductivity of the Ni foam substrate, decreasing the charge transfer barrier at the electrode interface,[36] and to the higher catalyst surface area originating from the Ni foam 3D structure (see Figure 5a and Figure S7, Supporting Information).

Whereas MnO_2 deposition lowered the Ni foam overpotential by ≈ 60 mV (see Figure 6), the subsequent functionalization with Co_3O_4 or Fe_2O_3 further decreased this value by 10 and 30 mV, respectively. A reasonable explanation for such trend is the enhanced catalytic activity of MnO_2-based samples compared to the bare Ni foam, as indeed revealed by Tafel slope values determined from Figure 6b.[44] For functionalized samples, in line with the above EIS data on FTO-supported specimens, further contributing effects responsible for the observed phenomenon can be related to an enhanced charge carriers separation at the Co_3O_4/MnO_2 and Fe_2O_3/MnO_2 interfaces,[52] as well as to the intrinsic catalytic activity of cobalt and iron oxides,[38,39,53] and the higher concentration (≈ +10%) of surface oxygen defects (see above and Figure S1b, Supporting Information).[17]

Among the developed materials, the Fe_2O_3/MnO_2 sample showed one of the highest activities (in terms of current density and Tafel slope values) ever reported in OER processes over MnO_x-based systems (compare Fig. 6 and Table S1). Furthermore, Tafel slope values

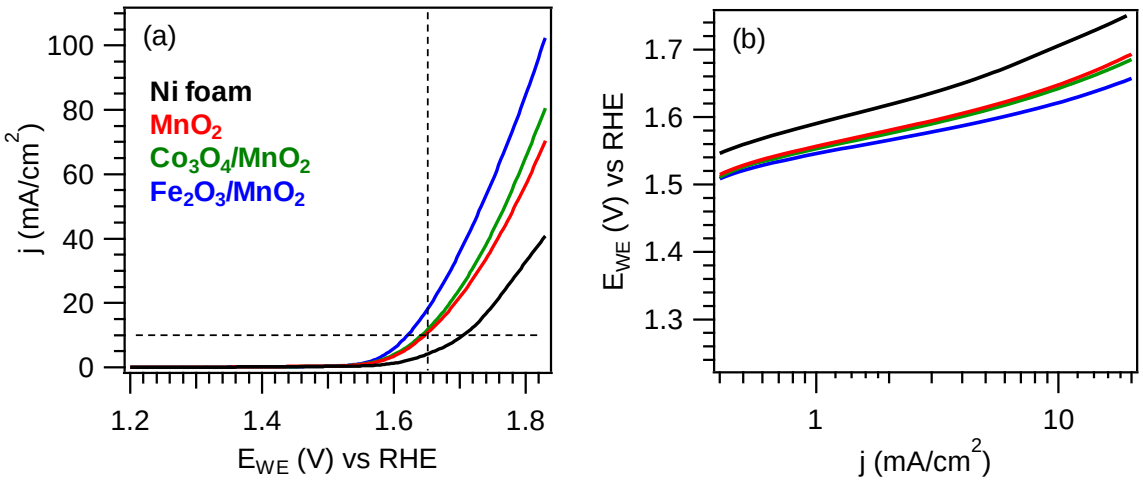

Sample	j @ 1.65 V (mA/cm^2)	η @ 10 mA/cm^2 (mV)	Tafel slope (mV/decade)
Ni foam	4.0	480	99
MnO_2	10.4	420	83
Co_3O_4/MnO_2	11.5	410	79
Fe_2O_3/MnO_2	17.9	390	69

Figure 6. (a) LSV curves (under dark) and (b) Tafel plots for MnO_2-based samples on Ni foam. The bare substrate was also tested for comparison. Current densities (j) at 1.65 V, overpotentials (η) at 10 mA/cm^2, and Tafel slope values are also reported in the table.

compared favorably, and often outperformed, the ones reported in the literature for IrO_2 and RuO_2, the benchmark materials for OER applications (see Table S2). Overall, despite that in some cases IrO_2 and RuO_2 materials performed better, such data confirms the potential of the synthetic strategy adopted in this work towards obtaining highly active OER catalysts. The best performing Fe_2O_3/MnO_2 specimen benefits not only from the favorable characteristics of the used substrate (compare Figure 4 and 6), but also from the enhanced in-depth dispersion of Fe_2O_3 NPs into the MnO_2 deposit compared to Co_3O_4/MnO_2 (see above). As a consequence, a higher density of heterojunctions and a more intimate Fe_2O_3/MnO_2 contact is achieved. These material features result, in turn, in an enhanced charge carrier separation at the Fe_2O_3/MnO_2 interface, favoring the delivery of electrons and holes to the external circuit and to the anode/electrolyte interface, respectively. In addition, despite the intrinsic catalytic

activity of bare iron oxides is typically lower than bare cobalt oxides, when iron oxides are used as functionalizing species a higher activity improvement occurs,[38-40] as indeed suggested by the above reported Tafel slope and overpotential values.

3. Conclusions

In this work, nanostructured electrode materials with *ad-hoc* properties based on *β*-MnO_2, the most stable manganese dioxide polymorph, were designed and developed by an original plasma-assisted strategy. Specifically, *β*-MnO_2 was deposited both on standard FTO glass supports and on highly porous Ni foams by PE-CVD, and subsequently decorated with Co_3O_4 or Fe_2O_3 nanoparticles by means of RF-sputtering. The aim of this approach was to investigate the synergistic influence exerted on functional performances by both the used substrate, and the chemical/electronic interplay between the *pyrolusite* matrix and the introduced surface species. The inherent advantages of the adopted synthetic approach enabled the fabrication of high-purity systems, characterized by an intimate contact between MnO_2 and Co_3O_4 or Fe_2O_3. The developed materials were ultimately tested as anodes for (photo)electrocatalytic OER processes using alkaline freshwater as reaction medium. Remarkably, the combined control over substrate properties and *pyrolusite* surface engineering yielded, for the best performing Fe_2O_3/MnO_2 specimen on Ni foam, a dark current density of 17.9 mA/cm^2 at 1.65 V *vs*. RHE, an overpotential as low as 390 mV, and a Tafel slope of 69 mV/decade. Such values are among the best ever reported for manganese oxide-bases systems and compare favorably even with state-of-the-art IrO_2 and RuO_2 catalysts. The present work, providing the first literature example on surface-engineered *β*-MnO_2 systems on Ni-foam scaffolds for OER applications, paves the way to the future development of cost-effective devices for sustainable energy generation. In addition, the proposed preparation route to composite nanomaterials opens the door to the fabrication of highly efficient and low-cost electrodes even for the splitting of seawater, the most abundant water

reservoir on Earth, and for electrochemical processes involving the valorization of biomass derivatives (*e.g.* ethanol). Research efforts along this direction are already under way.

4. Experimental Section

Synthesis: PE-CVD of MnO_2 was performed on suitably pre-cleaned[19,73] FTO-coated glass substrates (Aldrich®; ≈ 7 Ω/sq; FTO thickness ≈ 600 nm) and Ni foam supports (Ni-4753, RECEMAT BV) using a custom-built plasmochemical reactor equipped with a radio frequency (RF) generator (ν = 13.56 MHz).[49] $Mn(hfa)_2TMEDA$ (hfa = 1,1,1,5,5,5-hexafluoro-2,4-pentanedionate; TMEDA = *N*,*N*,*N'*,*N'*-tetramethylethylenediamine),[48,74] was used as manganese molecular precursor. The compound was vaporized at 70 °C in an external glass reservoir and delivered into the reaction chamber by an electronic grade Ar flow (rate = 60 standard cubic centimeters per minute (sccm)) through gas lines maintained at 130 °C. Two separate inlets were used to introduce Ar (rate = 15 sccm) and electronic grade O_2 (rate = 5 sccm) directly into the reaction chamber. After preliminary optimization experiments, the total pressure, RF-power, and growth temperature were set at 1.0 mbar, 20 W, and 300 °C, respectively, whereas the MnO_2 deposition time was fixed at 1 h and 3 h over FTO and Ni foam substrates.

The preparation of functionalized MnO_2-based systems was carried out by RF-sputtering in the same reactor used for PE-CVD experiments. To this aim, cobalt (Neyco®, 99.99%) and iron (Alfa Aesar®, 99.995%) metal targets were used for the fabrication of Co_3O_4/MnO_2 and Fe_2O_3/MnO_2 systems. Sputtering processes were carried out from pure Ar plasmas (rate = 10 sccm) at 0.3 mbar, 20 W and 60 °C, adopting a process duration of 2 h and 3 h for cobalt and iron deposition, respectively. The resulting materials were finally annealed *ex-situ* in air at 500 °C for 1 h.

Characterization: XRD patterns were collected at an incidence angle of 1.0° on a Bruker D8 Advance diffractometer, equipped with a Göbel mirror and a Cu Kα X-ray source (40 kV, 40 mA).

XPS analyses were run on a Perkin–Elmer Φ 5600ci spectrometer using a standard Al Kα source (1486.6 eV). BE values were referenced to the adventitious C1s signal at 284.8 eV.

After a Shirley-type background subtraction, atomic percentages (at.%) were evaluated using Φ V5.4A sensitivity factors. When necessary, peak fitting was carried out by a least-squares procedure, using Gaussian–Lorentzian peak shapes. Cobalt and iron surface molar fractions were calculated as X_M = ((M at.%) / (M at.% + Mn at.%)×100),[37] with M = Co, Fe.

SIMS depth profiles were obtained on a Cameca IMS 4f mass spectrometer, using a Cs^+ primary beam (14.5 keV, 20 nA) and negative secondary ion detection. An electron gun was used to compensate for charging effects. Measurements were performed rastering over a 150×150 μm^2 area and sampling secondary ions from a sub-region close to 7×7 μm^2 to avoid crater effects. In order to improve in-depth resolution and avoid possible mass interference artifacts, beam blanking mode and high mass resolution configuration were adopted.

An aberration corrected FEI Titan3 transmission electron microscope operated at an acceleration voltage of 300 kV was used for HAADF-STEM, SAED, EDXS and EELS analysis. Samples were prepared using Ga-focused ion beam milling on a FEI Helios Nanolab 650 followed by an *in-situ* lift-out step using an omniprobe, and further fine thinning step at 8 kV and, finally, 2 kV ion beam energy, to obtain electron transparent samples with sub-100 nm thickness.

FE-SEM measurements were performed on a Zeiss SUPRA 40VP microscope, at acceleration voltages between 10 kV and 20 kV. The ImageJ® software (http://imagej.nih.gov/ij/) was used to estimate deposit thickness and aggregate size.

Optical absorption spectra were recorded in transmittance mode at normal incidence on a Varian Cary 50 spectrophotometer, using bare FTO-coated glass substrate as a reference. The band gap (E_G) of the samples was determined by Tauc plots assuming the occurrence of direct allowed transitions.[11,19,28]

Functional tests: Electrochemical and photoelectrochemical LSV measurements were conducted in a computer-controlled potentiostat (VMP3, BioLogic Science Instruments) with a three-electrode set-up. The counter electrode, reference electrode, and working electrodes

were a Pt mesh, an Hg/HgO electrode, and the target materials (1 cm^2 geometric area), respectively. A KOH solution was used as electrolyte (0.5 M and 1.0 M in case of FTO- and Ni-supported samples, respectively).

Potentials were converted into the reversible hydrogen electrode (RHE) scale according to the relation:

$$E_{RHE} = E_{Hg/HgO} + 0.0592 \times pH + 0.111 \quad (2)$$

EIS measurements were carried out both in the dark and under illumination in the 100 mHz - 200 kHz frequency range at different applied biases, with an alternate current (AC) perturbation of 10 mV in amplitude. Nyquist plots (imaginary *vs*. real components of impedance, -Im(Z) *vs*. Re(Z)) were fitted to the corresponding equivalent circuits using ZView software (Scribner Associates, v. 3.2b).

Measurements under illumination were performed using a 150 W AM 1.5G solar simulator (Solar Light Co., 16S-300-002 v 4.0). The incident light intensity of 2 Sun (200 mW cm^{-2}) was measured through a thermopile (Gentec-EO, XLPF12-3S-H2-DO) coupled with an optical power meter (Gentec-EO UNO). In all cases, the electrode was irradiated from the front side (electrode-electrolyte interface).

Supporting Information
Supporting Information is available from the Wiley Online Library or from the author.

Acknowledgements

This work has been financially supported by Padova University DOR 2017–2019, P-DiSC #03BIRD2016-UNIPD and #03BIRD2018-UNIPD projects. A.G. acknowledges AMGA Foundation and INSTM Consortium. J.V. gratefully acknowledges funding from the GOA project “Solarpaint” of the University of Antwerp and the European Union's Horizon 2020 research and innovation programme under grant agreement No 823717 – ESTEEM3.

Received: ((will be filled in by the editorial staff))
Revised: ((will be filled in by the editorial staff))
Published online: ((will be filled in by the editorial staff))

References

[1] M. Fekete, R. K. Hocking, S. L. Y. Chang, C. Italiano, A. F. Patti, F. Arena, L. Spiccia, *Energy Environ. Sci.* **2013**, *6*, 2222-2232.

[2] Y. T. Meng, W. Q. Song, H. Huang, Z. Ren, S. Y. Chen, S. L. Suib, *J. Am. Chem. Soc.* **2014**, *136*, 11452-11464.

[3] M. Tahir, L. Pan, F. Idrees, X. Zhang, L. Wang, J.-J. Zou, Z. L. Wang, *Nano Energy* **2017**, *37*, 136-157.

[4] N. K. Chaudhari, H. Jin, B. Kim, K. Lee, *Nanoscale* **2017**, *9*, 12231-12247.

[5] C. E. Frey, P. Kurz, *Chem. Eur. J.* **2015**, *21*, 14958-14968.

[6] Z. Y. Li, S. T. Shi, Q. S. Zhong, C. J. Zhang, C. W. Xu, *Electrochim. Acta* **2014**, *146*, 119-124.

[7] D. M. Robinson, Y. B. Go, M. Mui, G. Gardner, Z. Zhang, D. Mastrogiovanni, E. Garfunkel, J. Li, M. Greenblatt, G. C. Dismukes, *J. Am. Chem. Soc.* **2013**, *135*, 3494-3501.

[8] C.-H. Kuo, W. Li, L. Pahalagedara, A. M. El-Sawy, D. Kriz, N. Genz, C. Guild, T. Ressler, S. L. Suib, J. He, *Angew. Chem. Int. Ed.* **2015**, *54*, 2345-2350.

[9] H. Kakizaki, H. Ooka, T. Hayashi, A. Yamaguchi, N. Bonnet-Mercier, K. Hashimoto, R. Nakamura, *Adv. Funct. Mater.* **2018**, *28*, 1706319.

[10] H. Ooka, T. Takashima, A. Yamaguchi, T. Hayashi, R. Nakamura, *Chem. Commun.* **2017**, *53*, 7149-7161.

[11] J. Rossmeisl, Z. W. Qu, H. Zhu, G. J. Kroes, J. K. Nørskov, *J. Electroanal. Chem.* **2007**, *607*, 83-89.

[12] Z. Geng, Y. Wang, J. Liu, G. Li, L. Li, K. Huang, L. Yuan, S. Feng, *ACS Appl. Mater. Interfaces* **2016**, *8*, 27825-27831.

[13] M. Q. Yu, Y. H. Li, S. Yang, P. F. Liu, L. F. Pan, L. Zhang, H. G. Yang, *J. Mater. Chem. A* **2015**, *3*, 14101-14104.

[14] X. P. Li, J. Liu, Y. H. Zhao, H. J. Zhang, F. P. Du, C. Lin, T. J. Zhao, Y. H. Sun, *ChemCatChem* **2015**, *7*, 1848-1856.

[15] F. Mattelaer, P. M. Vereecken, J. Dendooven, C. Detavernier, *Chem. Mater.* **2015**, *27*, 3628-3635.

[16] M. Yang, D. S. Kim, J.-W. Sim, J.-M. Jeong, D. H. Kim, J. H. Choi, J. Kim, S.-S. Kim, B. G. Choi, *Appl. Surf. Sci.* **2017**, *407*, 540-545.

[17] A. Ramírez, P. Hillebrand, D. Stellmach, M. M. May, P. Bogdanoff, S. Fiechter, *J. Phys. Chem. C* **2014**, *118*, 14073-14081.

[18] N. Kumar, A. Sen, K. Rajendran, R. Rameshbabu, J. Ragupathi, H. A. Therese, T. Maiyalagan, *RSC Adv.* **2017**, *7*, 25041-25053.

[19] D. Barreca, F. Gri, A. Gasparotto, G. Carraro, L. Bigiani, T. Altantzis, B. Žener, U. Lavrenčič Štangar, B. Alessi, D. B. Padmanaban, D. Mariotti, C. Maccato, *Nanoscale* **2019**, *11*, 98-108.

[20] V. B. R. Boppana, S. Yusuf, G. S. Hutchings, F. Jiao, *Adv. Funct. Mater.* **2013**, *23*, 878-884.

[21] F. Liu, M. Zeng, Y. Z. Li, Y. Yang, M. Y. Mao, X. J. Zhao, *Adv. Funct. Mater.* **2016**, *26*, 4518-4526.

[22] K. Saravanakumar, V. Muthuraj, S. Vadivel, *RSC Adv.* **2016**, *6*, 61357-61366.

[23] A. Gasparotto, C. Maccato, A. Petala, S. Bebelis, C. Sada, D. I. Kondarides, D. Barreca, *ACS Appl. Energy Mater.* **2019**, *2*, 8294-8302.

[24] C. E. Frey, F. Kwok, D. Gonzáles-Flores, J. Ohms, K. A. Cooley, H. Dau, I. Zaharieva, T. N. Walter, H. Simchi, S. E. Mohney, P. Kurz, *Sustain. Energy Fuels* **2017**, *1*, 1162-1170.

[25] J. Horkans, *J. Electrochem. Soc.* **1977**, *124*, 1202.

[26] Y. Matsumoto, E. Sato, *Mat. Chem. Phys.* **1986**, *14*, 397-426.

[27] B. A. Pinaud, Z. B. Chen, D. N. Abram, T. F. Jaramillo, *J. Phys. Chem. C* **2011**, *115*, 11830-11838.

[28] T. D. Dang, A. N. Banerjee, Q. T. Tran, S. Roy, *J. Phys. Chem. Solids* **2016**, *98*, 50-58.

[29] Z. X. Pei, M. S. Zhu, Y. Huang, Q. Xue, H. Y. Geng, C. Y. Zhi, *Nano Energy* **2016**, *20*, 254-263.

[30] W. Tang, M. Yao, Y. Deng, X. Li, N. Han, X. Wu, Y. Chen, *Chem. Eng. J.* **2016**, *306*, 709-718.

[31] J. M. Li, Z. P. Qu, Y. Qin, H. Wang, *Appl. Surf. Sci.* **2016**, *385*, 234-240.

[32] L. Jiang, G. Zhang, D. Li, C. Liu, S. Xing, *New J. Chem.* **2019**, *43*, 16870-16875.

[33] W. Zhu, R. Zhang, F. Qu, A. M. Asiri, X. Sun, *ChemCatChem* **2017**, *9*, 1721-1743.

[34] A. R. Merritt, R. Rajagopalan, J. D. Carter, *Thin Solid Films* **2014**, *556*, 28-34.

[35] J. Y. Kim, H. Jun, S. J. Hong, H. G. Kim, J. S. Lee, *Int. J. Hydrogen Energy* **2011**, *36*, 9462-9468.

[36] N. Bhandary, A. P. Singh, P. P. Ingole, S. Basu, *RSC Adv.* **2016**, *6*, 35239-35247.

[37] G. Carraro, A. Gasparotto, C. Maccato, E. Bontempi, D. Barreca, *Surf. Coat. Technol.* **2016**, *307*, 352-358.

[38] F. Song, L. Bai, A. Moysiadou, S. Lee, C. Hu, L. Liardet, X. Hu, *J. Am. Chem. Soc.* **2018**, *140*, 7748-7759.

[39] J. R. Galán-Mascarós, *ChemElectroChem* **2015**, *2*, 37-50.

[40] Y. Cheng, S. P. Jiang, *Prog. Nat. Sci.: Mater. International* **2015**, *25*, 545-553.

[41] A. Gasparotto, D. Barreca, C. Maccato, E. Tondello, *Nanoscale* **2012**, *4*, 2813-2825.

[42] C. Maccato, D. Barreca, G. Carraro, A. Gasparotto, V. Gombac, P. Fornasiero, *Surf. Coat. Technol.* **2013**, *230*, 219-227.

[43] D. Bekermann, D. Barreca, A. Gasparotto, C. Maccato, *CrystEngComm* **2012**, *14*, 6347-6358.

[44] M. Huynh, C. Shi, S. J. L. Billinge, D. G. Nocera, *J. Am. Chem. Soc.* **2015**, *137*, 14887-14904.

[45] R. Naeem, M. A. Ehsan, R. Yahya, M. Sohail, H. Khaledi, M. Mazhar, *Dalton Trans.* **2016**, *45*, 14928-14939.

[46] Z. Morgan Chan, D. A. Kitchaev, J. Nelson Weker, C. Schnedermann, K. Lim, G. Ceder, W. Tumas, M. F. Toney, D. G. Nocera, *PNAS* **2018**, *115*, E5261-E5268.

[47] Pattern N°024-0735, JCPDS (2000).

[48] D. Barreca, G. Carraro, E. Fois, A. Gasparotto, F. Gri, R. Seraglia, M. Wilken, A. Venzo, A. Devi, G. Tabacchi, C. Maccato, *J. Phys. Chem. C* **2018**, *122*, 1367-1375.

[49] D. Barreca, F. Gri, A. Gasparotto, T. Altantzis, V. Gombac, P. Fornasiero, C. Maccato, *Inorg. Chem.* **2018**, *57*, 14564-14573.

[50] D. Barreca, E. Comini, A. Gasparotto, C. Maccato, A. Pozza, C. Sada, G. Sberveglieri, E. Tondello, *J. Nanosci. Nanotechnol.* **2010**, *10*, 8054-8061.

[51] W. G. Sunda, S. A. Huntsman, G. R. Harvey, *Nature* **1983**, *301*, 234-236.

[52] Y. Xu, A. Li, T. Yao, C. Ma, X. Zhang, J. H. Shah, H. Han, *ChemSusChem* **2017**, *10*, 4277-4305.

[53] F. Lyu, Q. Wang, S. M. Choi, Y. Yin, *Small* **2019**, *15*, 1804201.

[54] M. E. G. Lyons, M. P. Brandon, *J. Electroanal. Chem.* **2009**, *631*, 62-70.

[55] R. L. Doyle, M. E. G. Lyons, *Phys. Chem. Chem. Phys.* **2013**, *15*, 5224-5237.

[56] P. Tang, H. Xie, C. Ros, L. Han, M. Biset-Peiró, Y. He, W. Kramer, A. P. Rodríguez, E. Saucedo, J. R. Galán-Mascarós, T. Andreu, J. R. Morante, J. Arbiol, *Energy Environ. Sci.* **2017**, *10*, 2124-2136.

[57] D. Monllor-Satoca, M. Bärtsch, C. Fàbrega, A. Genç, S. Reinhard, T. Andreu, J. Arbiol, M. Niederberger, J. R. Morante, *Energy Environ. Sci.* **2015**, *8*, 3242-3254.

[58] Q. Shi, S. Murcia-López, P. Tang, C. Flox, J. R. Morante, Z. Bian, H. Wang, T. Andreu, *ACS Catal.* **2018**, *8*, 3331-3342.

[59] D. A. Harrington, B. E. Conway, *Electrochim. Acta* **1987**, *32*, 1703-1712.

[60] M. Yu, G. Moon, E. Bill, H. Tüysüz, *ACS Appl. Energy Mater.* **2019**, *2*, 1199-1209.

[61] S. M. Sze, K. K. Ng, *Physics of semiconductor devices*, John Wiley & Sons, Inc., 3rd Ed., 2007.

[62] Y. Zhao, C. Chang, F. Teng, Y. Zhao, G. Chen, R. Shi, G. I. N. Waterhouse, W. Huang, T. Zhang, *Adv. Energy Mater.* **2017**, *7*, 1700005.

[63] C. Liang, P. Zou, A. Nairan, Y. Zhang, J. Liu, K. Liu, S. Hu, F. Kang, H. J. Fan, C. Yang, *Energy Environ. Sci.* **2020**, *13*, 86-95.

[64] I. Zaharieva, P. Chernev, M. Risch, K. Klingan, M. Kohlhoff, A. Fischer, H. Dau, *Energy Environ. Sci.* **2012**, *5*, 7081-7089.

[65] R. K. Hocking, R. Brimblecombe, L.-Y. Chang, A. Singh, M. H. Cheah, C. Glover, W. H. Casey, L. Spiccia, *Nat. Chem.* **2011**, *3*, 461-466.

[66] W. G. Sunda, S. A. Huntsman, *Mar. Chem.* **1994**, *46*, 133-152.

[67] M. Sharon, *An Introduction to the Physics and Electrochemistry of Semiconductors*, Wiley, 2016.

[68] R. B. Gupta, *Hydrogen Fuel: Production, Transport, and Storage*, CRC Press, 2008.

[69] A. Baral, D. P. Das, M. Minakshi, M. K. Ghosh, D. K. Padhi, *ChemistrySelect* **2016**, *1*, 4277-4285.

[70] PDF Card N°39-1346.

[71] G. Carraro, C. Maccato, A. Gasparotto, K. Kaunisto, C. Sada, D. Barreca, *Plasma Processes Polym.* **2016**, *13*, 191-200.

[72] H. Tan, J. Verbeeck, A. Abakumov, G. Van Tendeloo, *Ultramicroscopy* **2012**, *116*, 24-33.

[73] Z. Li, M. Shao, H. An, Z. Wang, S. Xu, M. Wei, D. G. Evans, X. Duan, *Chem. Sci.* **2015**, *6*, 6624-6631.

[74] C. Maccato, L. Bigiani, G. Carraro, A. Gasparotto, R. Seraglia, J. Kim, A. Devi, G. Tabacchi, E. Fois, G. Pace, V. Di Noto, D. Barreca, *Chem. Eur. J.* **2017**, *23*, 17954-17963.